PAPER

Synthesis and characterization of α-Fe$_2$O$_3$ nanoparticles showing potential applications for sensing quaternary ammonium vapor at room temperature

To cite this article: Luis T Quispe *et al* 2022 *Nanotechnology* **33** 335704

View the article online for updates and enhancements.

Synthesis and characterization of α-Fe$_2$O$_3$ nanoparticles showing potential applications for sensing quaternary ammonium vapor at room temperature

Luis T Quispe[1,*] , **L G Luza Mamani**[1], **A A Baldárrago-Alcántara**[1] ,
L León Félix[1] , **Gerardo F Goya**[2], **J A Fuentes-García**[2] ,
D G Pacheco-Salazar[1] **and J A H Coaquira**[3,*]

[1] Laboratorio de Películas Delgadas, Escuela Profesional de Física, Universidad Nacional de San Agustín de Arequipa, Av. Independencia s/n, Arequipa, Perú
[2] Instituto de Nanociencia y Materiales de Aragón (INMA), CSIC-Universidad de Zaragoza, 50018 Zaragoza, Spain & Departamento de Física de la Materia Condensada, Facultad de Ciencias, Universidad de Zaragoza, E-50009 Zaragoza, Spain
[3] Laboratory of Magnetic Characterization, Instituto de Física, Universidade de Brasília, DF 70910-900, Brasília, Brazil

E-mail: l.torre.q@gmail.com and coaquira@unb.br

CrossMark

Abstract

P-type and n-type metal oxide semiconductors are widely used in the manufacture of gas sensing materials, due to their excellent electronic, electrical and electrocatalytic properties. Hematite (α-Fe$_2$O$_3$) compound has been reported as a promising material for sensing broad types of gases, due to its affordability, good stability and semiconducting properties. In the present work, the efficient and easy-to-implement sol-gel method has been used to synthesize α-Fe$_2$O$_3$ nanoparticles (NPs). The TGA-DSC characterizations of the precursor gel provided information about the phase transformation temperature and the mass percentage of the hematite NPs. X-ray diffraction, transmission electron microscopy and x-ray photoelectron spectroscopy data analyses indicated the formation of two iron oxide phases (hematite and magnetite) when the NPs are subjected to thermal treatment at 400 °C. Meanwhile, only the hematite phase was determined for thermal annealing above 500 °C up to 800 °C. Besides, the crystallite size shows an increasing trend with the thermal annealing and no defined morphology. A clear reduction of surface defects, associated with oxygen vacancies was also evidenced when the annealing temperature was increased, resulting in changes on the electrical properties of hematite NPs. Resistive gas-sensing tests were carried out using hematite NPs + glycerin paste, to detect quaternary ammonium compounds. Room-temperature high sensitivity values ($S_r \sim 4$) have been obtained during the detection of $\sim$1 mM quaternary ammonium compounds vapor. The dependence of the sensitivity on the particle size, the mass ratio of NPs with respect to the organic ligand, changes in the dielectric properties, and the electrical conduction mechanism of gas sensing was discussed.

Supplementary material for this article is available online

Keywords: hematite nanoparticles, quaternary ammonium compounds, room temperature gas sensor, sol-gel method

(Some figures may appear in colour only in the online journal)

---

* Authors to whom any correspondence should be addressed.

1. Introduction

Quaternary ammonium compounds (QACs) are organic substances whose antimicrobial properties are widely used against bacteria and viruses that cause mild infections such as colds and flu, to lethal infections such as COVID-19 caused by SARS-CoV-2. QACs are compounds approved for the disinfection of surfaces in several environments, both commercial and domestic, capable of eliminating from 99.9% to 99.999% of pathogenic bacteria and viruses [1], and even effective to eliminate/inactivate (>95%) microorganisms much more resistant to several drugs, such as *Staphylococcus aureus*, Enterococcus and Pseudomonas aeruginosa [2].

Although these compounds have been used for many years, supposedly safely, there are still some controversies today about whether the short or prolonged exposure to this product is not harmful to human or animal health, or whether the waste produced is friendly to the environment. Thus, we have on one side several studies comprising an extensive amount of data on QACs supporting their safe use in a variety of applications [3, 4], and on the other side, we have studies on the potential harm to human health, animals and the environment due to the use of this type of compounds [5, 6]. We can cite as an example a study published in Nature in which the negative effect provoked by these chemicals is evidenced when they were used for cleaning mice's cages, causing birth and fertility alterations [7]. Likewise, although these compounds are commonly used in a diluted form, the IPCS INCHEM (Chemical Safety Information from Intergovernmental Organizations) warns that their undiluted form can even cause burns to the skin and mucous membranes.

In recent years, after the identification of the SARS-CoV-2 virus as responsible for the COVID-19 outbreak, the EPA (U.S. Environmental Protection Agency) published a list of effective surface disinfectants in the fight against SARS-CoV-2, which until the Spring 2021 included 551 disinfectants, of which approximately 34% contained QACs, highlighting the importance of these compounds to public health during the pandemic [6]. Among the QACs, the ADBAC (Alkyl Dimethyl Benzyl Ammonium Chloride) and DDAC (Didecyl dimethyl ammonium chloride) compounds have the highest number of active records, which are the main ingredients of the fifth generation quaternary ammonium (5GQA) [8]. There are few reported works related to QACs sensors fast enough to avoid long exposure times that may degrade their performance, and therefore the development of new sensors allowing fast detection of QACs vapors is of practical interest. Moreover, these types of devices should be scaled up for mass production aiming for a low-cost and environmentally friendly process. The first QACs sensor was reported in 2009 and it was based on a colorimetric technique using a matrix formed by the inclusion of tricyclic basic dyes, capable of identifying and quantifying different quaternary ammonium salts [9]. More recently (2019) a novel sensor based on citrate-capped AgNPs immersed in an organic solvent, has been reported for the detection of mixed QACs in water samples via IR spectroscopy [10]. Among the currently used materials, the transition metal oxides show the greatest potential for the application of this type of sensors due to their electronic, electrical and electrocatalytic properties [11]. Metal oxide nanoparticles have been used for the detection of various gases, e.g. acetone sensors based on porous $NiFe_2O_4$ nanoparticles and core–shell-type $ZnCo_2O_4$ NPs. These materials were shown to be capable of detecting acetone concentrations as low as 30 ppm, with response times around 2 s and working temperatures of 250 °C and 200 °C, respectively [12, 13].

The hematite (α-Fe_2O_3) iron oxide is among the most stable n-type semiconducting oxides under environmental conditions. Due to its low production cost, high corrosion resistance, and environmentally friendly, different α-Fe_2O_3 nanostructures have been explored for applications as gas sensing devices [14–17]. Interestingly, large specific surface sensors made of α-Fe_2O_3 nanotubes have been reported to have detection limits for reducing vapors at least four times lower than the equivalent sensors based on α-Fe_2O_3 NPs [14]. It is important to note that one of the main hurdles in n-type semiconductor-based sensors is their longer response and recovery time, which have been improved by working with sensors based on α-Fe_2O_3 nanostructures such as porous microbars [16], which, although they have a high working temperature (200 °C–400 °C), present very high sensitivity values ($S \approx 8$) sensing ethanol, and response and recovery times less than 11 s. Likewise, sensors based on α-Fe2O3 nanostructures such as 3D leaf-like [17], hollow sea urchin-like, nanotubes and NPs [15], with working temperatures in the range of 200 °C–350 °C, present very high sensitivity values for a wide range of vapors and gases (ammonia, formaldehyde, triethylamine, acetone and ethanol), and low response (<50 s) and recovery (<20 s) times.

In all the devices mentioned above, the operating mechanism is such that their sensitivity is favored by both high temperature and specific surface area. This work show the design and prototyping of a low-cost chemiresistor tested as a sensor for QACs in the vapor phase, based on a novel operating mechanism. This sensor is composed of a three-dimensional assembly of hematite nanoparticles stabilized in an organic matrix of glycerin. The hematite has the advantage of its phase stability, low cost and good performance at room temperature. The glycerin matrix provided higher mechanical robustness to the device, as compared to the ethylene glycol matrix [18]. This device showed the capability of detecting concentrations of QACs vapors as low as 1.0 mM ($\sim$400 ppm) at room temperature.

2. Material and methods

2.1. Synthesis of nanoparticles

Hematite (α-Fe_2O_3) NPs were synthesized by the sol-gel method. To obtain $\sim$5 g of NPs, 5.0 g of commercial gelatin (unflavored sheets) was placed in a beaker and dissolved in $\sim$50 ml of distilled water (type II according to the ASTM International standard) at 70 °C during the magnetic stirring for a few minutes until the gelatin was completely dissolved.

Separately, 25.3 g of Fe(NO$_3$)$_3$.9H$_2$O (Sigma Aldrich, purity 99.9%) was dissolved in distilled water at room temperature and poured into the beaker containing the previously dissolved gelatin. The obtained mixture remained under magnetic stirring for ~7 h at 70 °C until the gel formation. Then, the obtained gel was subjected to an aging process by placing the sample in an oven at 70 °C to dry during ~24 h. In order to eliminate organic waste and to improve the crystallinity, the resulting aged sample was divided in lots, which were annealed at different temperatures (400 °C, 450 °C, 500 °C, 600 °C, 700 °C and 800 °C) during 3h and using a heating rate of 3.5 °C min^{-1}. The resulting samples were named S-400, S-450, S-500, S-600, S-700 and S-800, respectively, and the corresponding digital camera images are shown in figure S-1 (available online at stacks.iop.org/NANO/33/335704/mmedia) in the supplementary material.

2.2. Characterization techniques

Thermogravimetric analysis (TGA) and differential scanning calorimetry (DSC) measurements were carried out using a commercial instrument (TA Instruments, model SDT 650) to determine the phase transformation temperatures and the iron oxide nanoparticles content. Measurements were carried out under an air atmosphere from room temperature to 850 °C, using a heating rate of 10 °C min^{-1} and an initial sample amount of ~10 mg. The structural characterization of the NPs was carried out by x-ray diffraction (XRD) using a commercial diffractometer (Rigaku, Miniflex, model 600) with Cu-Kα radiation ($\lambda = 1.5418$ Å). The diffractograms were obtained in the 2θ range from 20 to 80°, with a step of 0.05°, using the Bragg-Brentano configuration. The diffractograms were further analyzed by the Rietveld refinement method, using GSAS (General Structure Analysis System) software. To obtain transmission electron microscopy (TEM) images, the NPs were dispersed in water by sonication during 5 min and, then, dropped onto a holey carbon-coated copper grid and dried in vacuum during 12 h. Bright-field and high-resolution TEM micrographs were obtained in a FEI Tecnai F30 microscope working with an accelerating voltage of 300 kV. Obtained images were processed using Digital Micrograph® software (GATAN®) for average diameter determination, and fast Fourier transform (FFT) was used for selected area electron diffraction (SAED) patterns simulation from high-resolution images. X-ray photoelectron spectroscopy (XPS) measurements were obtained using a Kratos AXIS Supra spectrometer, operated at an acceleration voltage of 15 kV and an emission current of 8 mA. The measurements were carried out at room temperature and in ultra-high vacuum conditions (working pressure below 10^{-7} Pa), using a monochromatic Al Kα radiation ($h\nu = 1486.6$ eV). The survey and high-resolution spectra were obtained with resolutions of 1.0 eV and 0.1 eV, respectively. During sample preparation, the NPs powder was mounted on the sample holder with double-sided tape, and the beam spot covered an area of ~1 mm^2.

2.3. Preparation of the sensors

Gas sensors based on NPs typically consist of films of NPs obtained by solvent evaporation, or mixed films consisting of NPs immersed in organic ligands. The film sensors used here were made from a paste obtained by mixing equal amounts (≈30 mg) of high purity glycerin and hematite NPs. The surface of a printed circuit with two interdigital electrodes was coated with the impregnation paste using the Doctor blade coating method. The geometric dimensions of the sensor were approximately 12 × 19 × 0.15 mm^3 with electrode spacing of 0.3 mm, as shown in figure 1(a). To stabilize and bind the active phase to the copper electrodes, the sensor was heated at 70 °C for approximately 24 h. Figure 1(b) shows a photograph of the actual film taken after this process.

2.4. Experimental set-up to test the sensors

The experimental setup shown in figure 2 was used for the sensitivity tests. The sensitivity system consisted of the following sections: (i) A feeding section, made up of a hermetic chamber where the volatile liquid (5GQA) is located. (ii) A detection section, made up of a hermetic chamber of fixed volume (balloon of 0.5 l), containing a commercial pressure and temperature sensor (BMP180) to monitor the gas partial pressure and working temperature in real-time. (iii) A control and data acquisition section, which is connected to the BMP180 and to the sensor material. The electrical connections of the pumps and valves are also in this section. Those connections allow the automatic control of feeding and cleaning processes during the tests. The electrical resistance of the gas sensor, temperature and pressure of the chamber are recorded in real-time using the Start Easy Expert software. All the sections are interconnected by a set of pipes, pumps and valves, which allow the automatic feeding and ventilation of the detection section during each cycle.

3. Results and discussion

3.1. TGA and DSC curves

The analysis of the TGA-DSC curves of the gel used to obtain the NPs is shown in figures 3(a), (b). The weight percent $W(\%)$ versus temperature (T) and dW/dT versus T plots, clearly indicate that the various thermal processes do not occur independently but rather simultaneously at different temperature ranges. The whole temperature range of 30 °C–850 °C showed four different processes taking place. In stage {1} (20 °C < T < 145 °C) a first ~8% weight loss takes place, which is mainly attributed to the evaporation [19, 20] or desorption [21] of water molecules adsorbed on the NP's surface, as well as the decomposition of a small portion of the organic compounds. In stage {2}, a rapid weight loss is produced by the decomposition (exothermic process) of organic material coming mainly from gelatin (exothermic peak at ~208 °C on the DSC curve). It corresponds to a weight loss of ~36.1 %, and occurs approximately in the range from 145 °C to 272 °C. In stage {3}, there is an additional weight loss of ~12.6 % in the range from 272 °C to 390 °C likely assigned to the
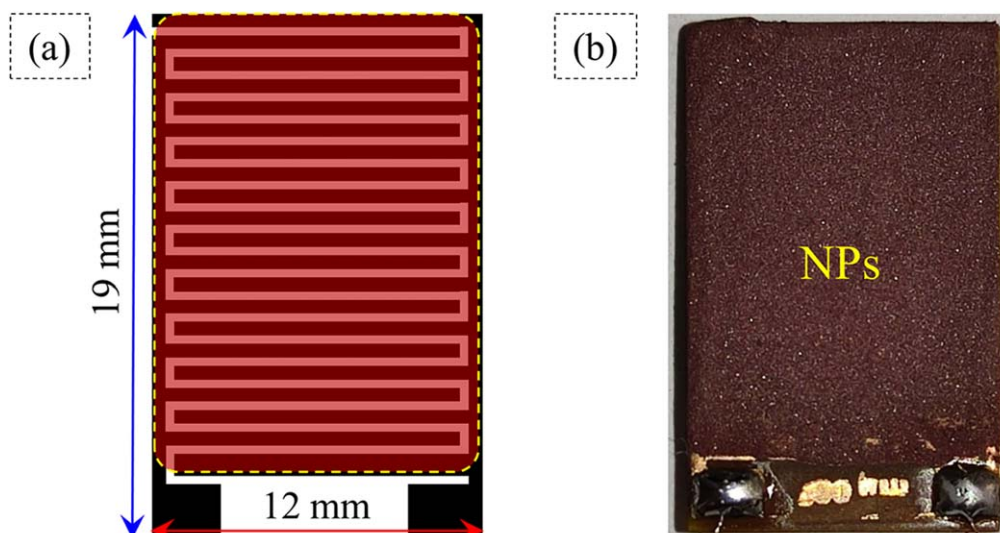
Figure 1. Schematic representation (a) and photograph (b) of the film sensor, which consists of a printed circuit with two copper electrodes, on which the mixture (NPs + glycerin) was deposited.
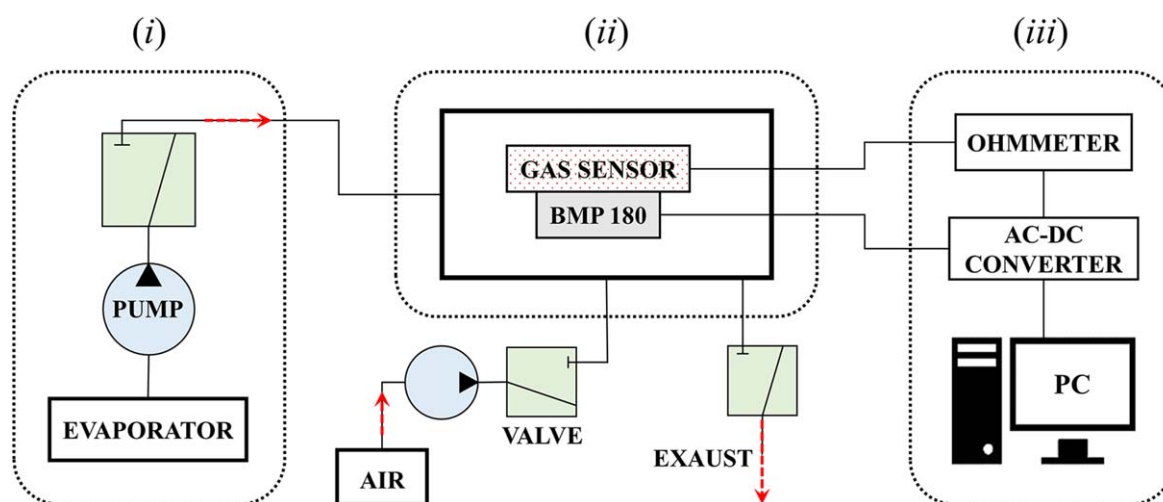

Figure 2. Experimental setup of the gas sensitivity system: (i) feeding section, (ii) detection section and (iii) control and data acquisition section.

oxidative decomposition of residual organic material coming mainly from metallic precursors, which occurs in the form of NO_x and CO_2 gas [22]. This process is also exothermic, as evidenced by the peak at ∼326 °C depicted in the DSC curve. In stage {4}, corresponding to the range from 390 °C to 840 °C, two main processes seem to occur. In the first process, there is a weight gain (evidenced by the peak in the dW/dT versus T curve at ∼509 °C) and it was associated with the phase transformation from γ-Fe_2O_3 to α-Fe_2O_3 [23, 24], in agreement with the exothermic peak observed in the DSC curve centered at ∼509 °C. This result is consistent with the XRD data analysis, which indicates the presence of only the α-Fe_2O_3 phase for samples annealed at temperatures at 450 °C and higher temperatures, as discussed below. It is worth mentioning that the phase transformation from Fe_3O_4 to γ-Fe_2O_3 which is expected to occur at temperatures ≈160 °C– 320 °C [25] could not be clearly observed in the TGA/DSC

curves, possibly obscured by the concurrent weight loss from the removal of organic compounds. The second process is mainly associated with the improvement of the crystallinity of hematite NPs and it corresponds to an exothermic process, as evidenced by the peak at ∼567 °C.

3.2. XRD data analysis

In figure 4(a), the obtained x-ray diffractograms from the elaborated samples at different thermal treatments are shown. For the sample annealed at 400 °C (sample S-400), the diffractogram reveals a polycrystalline structure as broad bands constitute the diffraction peaks. Is possible to identify α-Fe_2O_3 phase in the crystal structure thanks to the peaks associated with the planes (0 1 2), (1 0 4), (1 1 0), (1 1 3), (0 2 4), (1 1 6), (0 1 8), (2 1 4), (3 0 0), (1 0 10), (2 2 0) in the diffractogram; and also the Fe_3O_4 phase thanks to the peaks
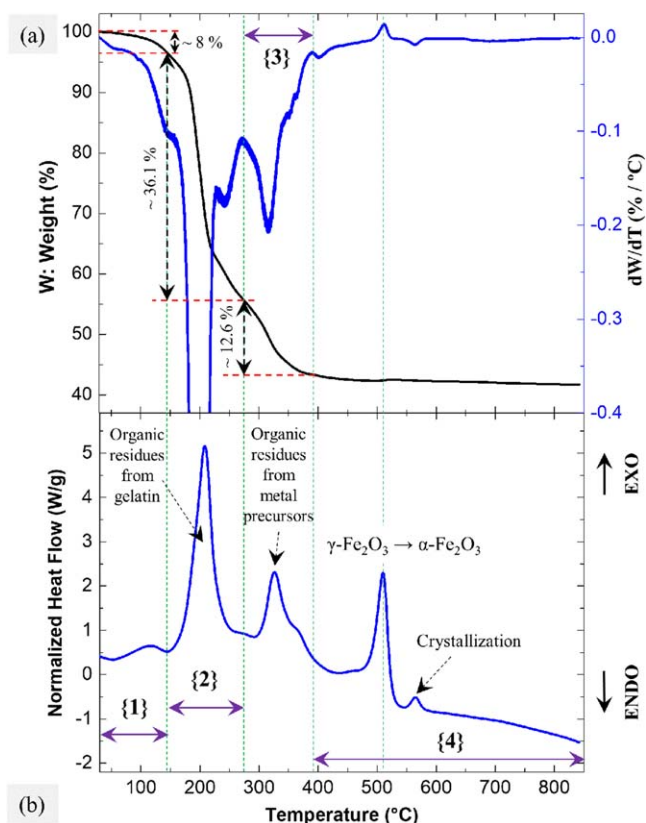
Figure 3. TGA (a) and DSC (b) curves of the gel used to obtain the hematite NPs. In (a) are shown the weight loss (*W*) versus temperature (*T*) and d*W*/d*T* versus *T* plots. The four stages discussed in the text are indicated.

associated with the planes (2 2 0), (3 1 1), (4 0 0), (4 4 0). On the other hand, for samples S-450, S-500, S-600, S-700 and S-800 annealed at higher temperatures the formation of single-phase α-Fe$_2$O$_3$ (H) was observed, confirming the phase transformation from the spinel Fe$_3$O$_4$ to rhombohedral α-Fe$_2$O$_3$ structure for annealing temperatures of 400 °C–450 °C.

Above that temperature range, better crystallinity was inferred from the narrowing of the Bragg reflection peaks. Detailed quantitative analysis from Rietveld refinement of the XRD patterns revealed the presence of ~38% of the α-Fe$_2$O$_3$ and ~62% of the Fe$_3$O$_4$ phase in sample S-400. The lattice constants of the hematite phase are $a = 5.03$ Å, $c = 13.75$ Å for the sample S-400 and remain unchanged for the other samples. The crystallite size (D_{XRD}) of both phases was calculated using the Scherrer relation. The obtained values are plotted in figure 4(b). A mean crystallite size $\langle D_{XRD} \rangle$ of ~8 nm is determined for the Fe$_3$O$_4$ phase (which is formed only in sample S-400). However, the $\langle D_{XRD} \rangle$ of the α-Fe$_2$O$_3$ phase shows a linear increasing trend with the annealing temperature, from ~18 nm (S-400) to ~40 nm (S-800).

3.3. Transmission electron microscopy (TEM)

In order to determine the morphology and compare particle size and structural properties of three selected samples, TEM
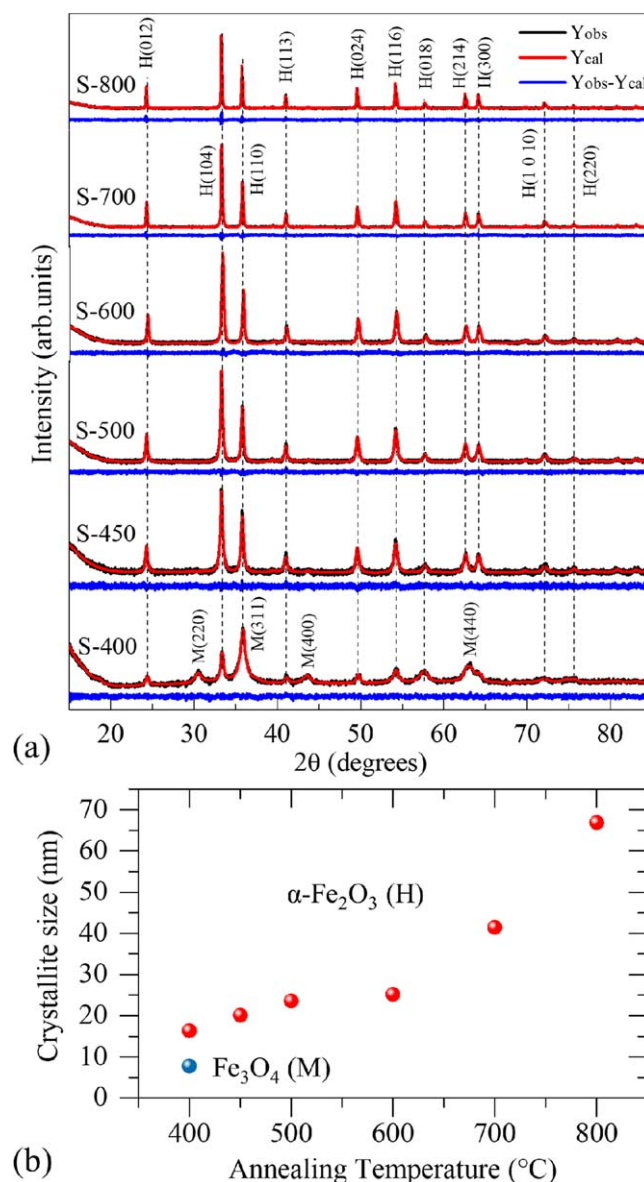
Figure 4. (a) X-ray diffractograms of the iron oxide nanoparticles refined using the Rietveld refinement method. The red solid line represents the calculated diffractograms and the black lines represent the experimental data; the blue line represents the difference between the experimental and calculated data. (b) Mean crystallite size as a function of the annealing temperature for the Fe$_3$O$_4$ and α-Fe$_2$O$_3$ phases.

analysis was performed. In figures 5(a)–(c), representative bright-field low-magnification images of S-400, S-600, and S-800 samples showed no distinctive morphologies. In order to mount the particle size histograms, the micrographs were used to account particle sizes using the DigitalMicrograph® software (GATAN®). In the insets are shown the histograms mounted according to the Sturges criteria [26]. The resulting histograms were fitted using a normal distribution function. Results provided average sizes of $D = 7.0 \pm 1.7$ nm, 28 ± 3 nm and 177 ± 34 nm for samples S-400, S-600 and S-800, respectively. These average diameter values are compatible with the crystallite size values obtained from the XRD data.
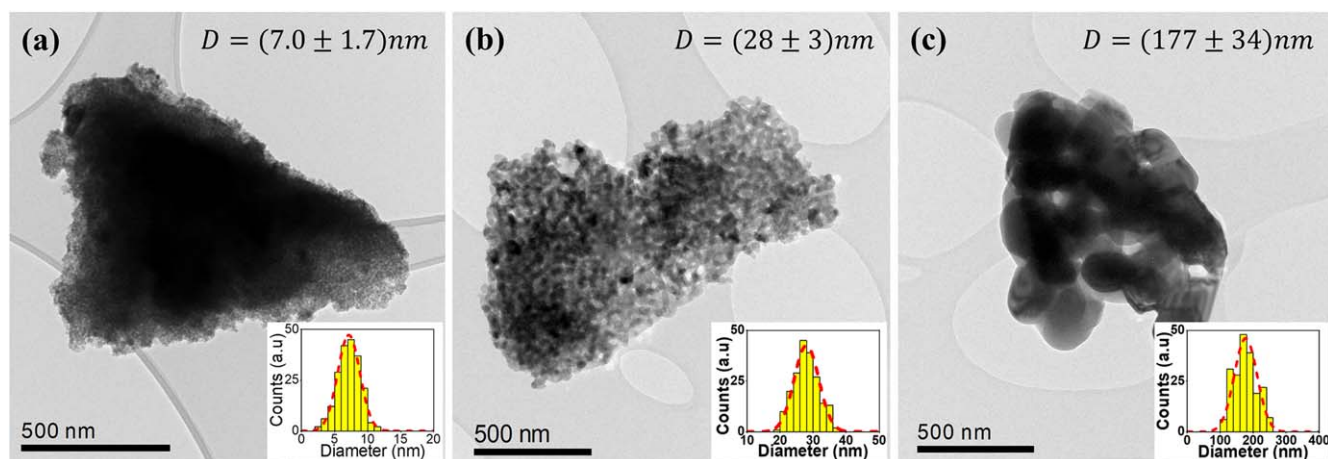
Figure 5. Low magnification bright-field TEM images of sample (a) S-400 (7.0 ± 1.7 nm), (b) S-600 (28 ± 3 nm), and (c) S-800 (177 ± 34 nm). The corresponding histograms are plotted in the insets, which were fitted to a normal distribution function.

The larger particle size from TEM compared to XRD values in sample S-800 in likely due to nanoparticle aggregation in this sample.

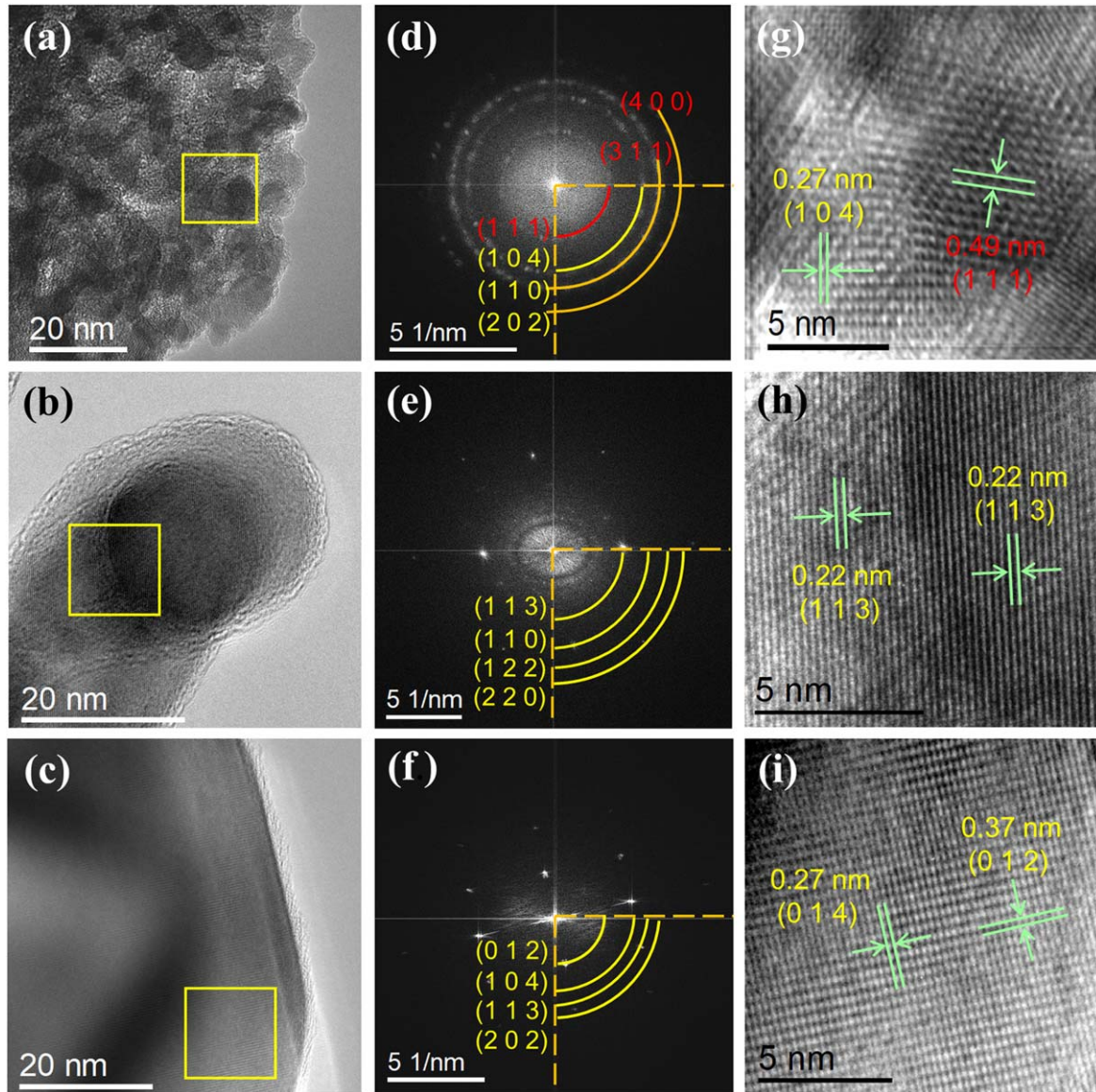High-resolution bright-field images (figure 6(a)) evidenced reduced crystallite sizes in sample S-400, while samples S-600 and S-800 showed larger crystallite sizes (figures 6(b), (c)). The FFT processing was done for SAED patterns simulation (figures 6(d)–(f)) to obtain the diffraction patterns with the respective indexation. For sample S-400 (figure 6(d)) the diffraction pattern showed several rings associated with polycrystalline material. Among these SAED patterns, it is possible to distinguish the crystal planes (1 1 1) assigned to the cubic Fe_3O_4 spinel phase, while the ring associated with the (1 0 4) plane corresponds to the α-Fe_2O_3 phase. Other overlapped rings are associated with the (1 1 0) and (2 0 2) planes of the α-Fe_2O_3 phase and rings associated with the (3 1 1) and (4 0 0) planes of the Fe_3O_4 phase, confirming the multiphase feature of sample S-400, according with the XRD data (figure 4(a)). Figures 6(e), (f) show diffraction patterns corresponding to a single-phase, α-Fe_2O_3. The diffraction pattern observed for the S-600 sample is associated with the family of planes (1 1 3), (1 1 0), (1 2 2) and (2 2 0), while the pattern for the sample S-800 is associated with the family of planes (0 1 2), (1 0 4), (1 1 3) and (2 2 0). The images in figures 6(g)–(i) are the zoom of the squares marked in figure 6(a)–(c), where the determined interplanar distances are indicated by the arrows. In the case of sample S-400, figure 6(g), the identified interplanar distance of 0.27 nm corresponds to the (1 0 4) planes of α-Fe_2O_3, and the interplanar distance of 0.49 nm corresponds to the (1 1 1) planes of Fe_3O_4. For sample S-600, figure 2(h), the interplanar distance of 0.22 nm corresponding to the (1 1 3) planes of α-Fe_2O_3 and no other planes were evidenced, even in the region between two particles. Finally, for the S-800 sample, figure 2(i) shows the interplanar distances of 0.27 and 0.37 nm, which correspond to the (0 1 4) and (0 1 2) planes of the α-Fe_2O_3 phase.

3.4. X-ray photoelectron spectroscopy (XPS)

XPS measurements allowed to determine the surface properties of the NPs regarding their phase composition and oxidation state (see figure S-2 in the supplementary material). For samples S-400, S-600 and S-800 only the peaks from the Fe, O and C edges could be identified. The high-resolution XPS spectra of C 1s (not shown) evidenced the presence of adventitious carbon (~284.6 eV) and carbonates (287.0 eV and 289.2 eV) in samples S-400 and S-600, but carbonates seem to disappear for sample S-800. The high-resolution O 1s XPS spectra are shown in figures 7(a)–(c). It is observed a predominant peak at ~529.8 eV (A1), which corresponds to the structural oxygen atoms from O–Fe bonds of the iron oxide phases. Likewise, the presence of a peak at 531.6 eV was also observed (A2), which was assigned to oxygen atoms related to O–C and O=C bonds, and even oxygen vacancies (V_O) [27–29]. The peak located at lower binding energy (528.2 eV) was assigned to instrumental artifacts according to the literature [29].

The high-resolution Fe 2p spectra are shown in figures 7(d)–(f). Data analysis revealed a peak at 710.2 eV which was assigned to the octahedrally coordinated Fe^{3+} ions of the hematite phase (S2). The peak centered at 709.1 eV (S1) is assigned to Fe^{2+} ions which occupy octahedral sites. Also, a peak located at 712.1 eV (S3) was assigned to tetrahedrally coordinated Fe^{3+} ions of the magnetite phase. The peak located at 706.2 eV was assigned to instrumental artifacts [29]. Moreover, its broad features can contain additional contributions coming from Fe-containing carbides [28]. Besides, the peaks at 709.1 and 712.1 eV in sample S-400 are expected due to the presence of the magnetite phase in that sample and they are not expected in the XPS spectra of samples S-600 and S-800, according to the XRD data analysis. However, those contributions observed in the XPS spectra of samples S-600 and S-800 could be related to the maghemite-like structure remaining at the surface of the particles or even small portions of magnetite (undetectable by the XRD technique) which survive heat treatments, as reported by Bora *et al* [30]. Data analysis indicates that the Fe content of the hematite phase increases as the annealing

Figure 6. High-resolution TEM characterizations. Bright-field images of samples S-400, S-600 and S-800 (a)–(c) were used to obtain simulated diffraction patterns, performed using FFT images (d)–(f). SAED analysis was performed from the selected area (square) of the bright-field images. Interplanar distances in the images (g)–(i) reveal the microstructure. In sample S-400 the presence of magnetite and hematite phases is evidenced, while in samples S-600 and S-800 only the hematite phase is determined.

temperature is increased as shown in table 1 (6th column), suggesting the crystallinity improvement of the hematite phase at higher annealing temperatures, in agreement with XRD data analysis.

3.5. Gas sensing measurements

The main parameters evaluated from our 5GQA vapor sensing tests were sensitivity, response time ($t_{response}$), and recovery time ($t_{recovery}$). The sensitivity of the gas sensing material is defined as the ratio of the sensor electrical resistance in air (R_a) to the resistance in the testing gas (R_v): $S_r = R_a/R_v$ or by the relative variation of the electrical resistance: $\Delta R/R_a$, both related as follows:

$$\frac{\Delta R}{R_a} = \frac{(R_v - R_a)}{R_a} = \frac{1}{S_r} - 1. \quad (1)$$

Although the QACs vapors do not have an ideal gas-type behavior, we assumed this simplifying hypothesis to estimate the concentration of vapor phases. The concentration was calculated from the expression $C = n/V = P/RT$, where n is the number of 5GQA moles contained in the chamber of volume (V), at a pressure P and a temperature T. R is the universal constant of ideal gases. Determining the concentration of these vapors in ppm can be complex because of uncertainties in the molecular weight of 5GQA components due to their varying compositional nature. However, considering that the molecular weights are within 340–400 g mol^{-1} range [31], we could estimate that the concentration of $C = 10^{-3}$ mol l^{-1} = 1 mM corresponds to approximately 400 ppm.

Figure 8(a) shows part of a sensitivity curve of the sensor based on the S-800 sample, which was obtained by alternating
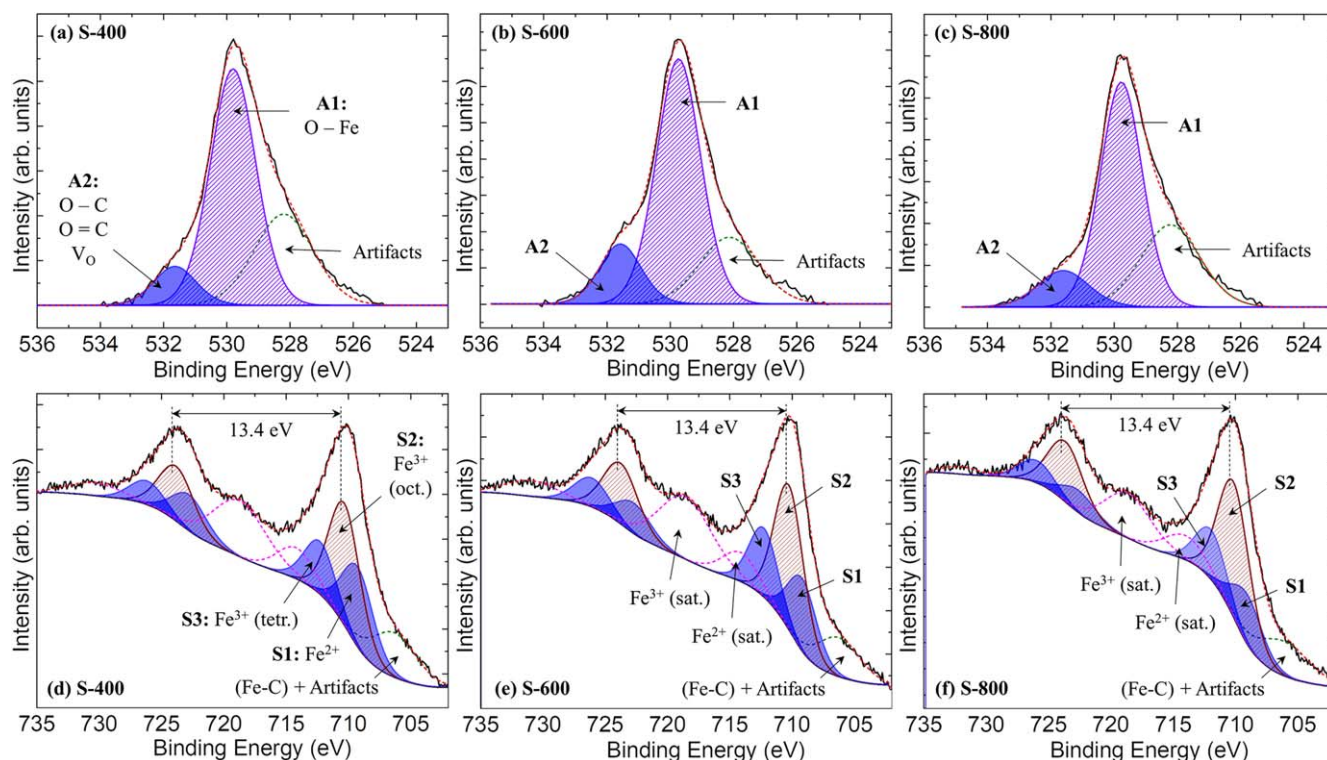
Figure 7. Deconvolutions of the high-resolution XPS spectra of O1s (a)–(c) and Fe2p (d)–(f).

the measurement between air (gray region) and $\sim$1.4 mM of 5GQA-vapor (white region). A measuring time of 10 min (5 min) in air (in 5GQA) was chosen for the measurement. The sensor electrical resistance value in each atmosphere (R_a and R_v) was determined when the electrical resistance reaches a stable value (steady region). Similar criteria (as shown in figure 8(a)) were used for measuring other 5GQA concentrations (from 0.8 to 4.0 mM). It is worth mentioning that the assessment of 5GQA in this range of concentrations is important due to the reported toxicity limit of humans and animals ($\sim$1 mM of QACs concentration) [32, 33]. The parameter $|\Delta R/R_a|$ shows a linear dependence on the 5GQA-vapor concentration (C) up to 4 mM, as shown in figure 8(b). The linear fit of data provides a relation of: $|\Delta R/R_a|$ [%] $\approx$ 19.274 $\times$ C[mM], and a correlation coefficient, $R^2 = 0.998$.

The sensitivity curves for the sensors based on the S-400, S-500, S-600, S-700 and S-800 samples are shown in figures 9(a)–(e), which were obtained for a 5GQA-vapor concentration of $C \approx 4$ mM. Although no perfect steady state was achieved in all samples, as can be seen in figures 9(b), (c) for samples S-500 and S-600, in order to determine the electrical resistances, response and recovery times, a measurement time of 10 min in air and 5 min in 5GQA vapor was chosen for all samples. The $|\Delta R/R_a|$ values of all samples are calculated using the curves shown in figures 9(a)–(e). As shown in figure 9(f), the value obtained for sample S-400 (containing two crystalline phases) is around 30%. Moreover, a systematic improvement in the sensitivity was observed for the annealed samples (single-phase samples). The $|\Delta R/R_a|$ values range from $\sim$25% for sample S-500 to $\sim$75% for

sample S-800, showing a linear trend with the annealing temperature as shown in figure 9(f). It is worth mentioning that the sensor based on S-800 sample showed more stable electrical resistance values, both in air and in the 5GQA-vapor. High sensitivity is usually expected in NPs-based sensors due to the high surface area-to-volume ratio, and that sensitivity becomes higher for smaller sized NPs. The hematite nanoparticles-based 5GQA sensor tested here showed an opposite trend, i.e. the sensitivity was higher for larger NPs sizes (larger annealing temperature). We believe that some particularities related to the operating mechanism will be responsible, as will be discussed in the next subsection.

Regarding t_{response} and t_{recovery}, the results obtained are shown graphically in figure 9(g). The t_{response} and t_{recovery} values obtained for sample S-400 are around 2.2 and 4.7 min, which is not a pure hematite sample. However, for the single-phase sample S-500 slightly larger values (3.5 and 8.1 min) are determined, and a decreasing trend for samples annealed at higher temperatures are obtained, becoming $t_{\text{response}} = 1.3$ min and $t_{\text{recovery}} = 3.8$ min for sample S-800, as shown in figure 9(g).

3.6. Sensing mechanism

The sensor studied in this work can basically be modeled as a three-dimensional (3D) assembly of semiconductor nanoparticles stabilized with organic ligands (glycerin). The electrical resistance of this system can be analyzed considering the model proposed by Neugebauer and Webb

Table 1. Atomic percentage (at%) values obtained from the high-resolution XPS spectra of O 1s (A1, A2) and Fe 2p (S1, S2 and S3).

O 1s				Fe 2p 3/2			
Samples	A1 (at%)	A2 (at%)	A2/(A1 + A2)	S1 (at%)	S2 (at%)	S3 (at%)	S2/(S1 + S2 + S3)
S-400	60.4	9.2	13.2%	25.3	38.1	16.6	47.6%
S-600	62.7	14.4	18.7%	21.3	42.0	20.1	50.4%
S-800	58.3	11.4	16.4%	17.2	46.0	17.1	57.3%

[34–36], commonly used for metallic systems. Within this model, two contributions to the overall resistivity: one associated with the electronic tunneling between two NPs dispersed in a dielectric, and the second contribution associated with the activation energy required to convert two initially neutral NPs into two charged NPs, one positive and one negative. Assuming that this model can be used to model our system, the following relationship is obtained for the overall electrical resistivity of the sensor,

$$\rho = \rho_0 \exp(\beta\delta) \exp\left(\frac{E_A}{k_B T}\right), \quad (2)$$

where β is the electron tunneling coefficient (in the order of 1 Å^{-1} for metals) [35], and considerably higher values are expected for semiconducting materials, δ is the inter-particle spacing (as shown in figure 10(b)), k_B is the Boltzmann constant, T is the sensor working temperature, E_A being the activation energy (named also as the charging energy). In the $E_A \ll k_B T$ regime, the resistivity is given by $\rho \approx \rho_0 \exp(\beta\delta)$.

Figure 10(a) shows a schematic representation of the sensor connected to a power source. Also, a diagram of a small region of the sensor (not to scale) in air (figure 10(b)) and in 5GQA vapor (figure 10(c)) are shown to provide a possible operating mechanism of the sensor. Due to the sensor geometry (figure 10(a)) its electrical resistance is proportional to its overall resistivity, the ratio of the electrical resistances $S_r = R_a/R_v$ can be expressed as,

$$S_r = \frac{R^{(a)}}{R^{(v)}} = \frac{\rho^{(a)}}{\rho^{(v)}} = \exp\left(\frac{E_A^{(a)} - E_A^{(v)}}{k_B T}\right) = \exp\left(\frac{\Delta E_A}{k_B T}\right), \quad (3)$$

where, the superscript (a) corresponds to air atmosphere and the superscript (v) corresponds to the 5GQA-vapor atmosphere. From the experimental values of S_r (second column in table 2), it is possible to determine the variation of the activation energy when the sensor material is in atmospheric air and in 5GQA vapor, according to the following expression:

$$\Delta E_A = E_A^{(a)} - E_A^{(v)} = k_B T \ln(S_r). \quad (4)$$

As observed, the calculated values of ΔE_A listed in the table 2 (third column) becomes larger as the sensitivity increases. Further analysis can be done, in order to understand this result. It is known that the activation energy E_A in this type of system depends not only on geometric parameters, but also on the dielectric properties of the organic ligand. Likewise, the sensing atmosphere can affect the dielectric properties of the organic ligand, therefore, the activation energy can change depending on the atmosphere in which the sensor

is located. Mathematically, the activation energy can be quantified using the following expression [34, 35];

$$E_A^{(atm)} = \frac{2N_A e^2}{\varepsilon_r^{(atm)} \varepsilon_0 D \left(1 + \frac{D}{2\delta}\right)}, \quad (5)$$

where $\varepsilon_r^{(atm)}$ is the dielectric constant of the organic ligand altered by the surrounding medium (atm). Note that, from equations (2), (3) and (5), the contribution of the NPs to the electrical resistance of the sensor is due to its electrical properties and its geometrical features; however, for sensitivity issues, the term $\exp(\beta\delta)$ cancels (equation (3)). Since this term is more associated with the electrical properties of the NPs (by means of the β parameter), we inferred that only the geometrical features of the NPs menain relevant for the sensitivity.

Likewise, we believe that another relevant factor that allows the efficient detection of 5GQA vapor is the own polar nature of its constituents. In figures 10(b) and (c) is presented a schematic representation of the electric fields generated in the sensor when it is in air $(\vec{E})$ and in the 5GQA vapor $(\vec{E} + \vec{E}')$, where $\vec{E}'$ is the field generated by the polarized molecules (cations and chlorides of the 5GQA vapor), which is opposite to $\vec{E}$, and simulates the response of a dielectric material.

First, we analyze the geometrical effect on the activation energy of the material sensor in atmospheric air. Considering an ideal case where the NPs are equally spaced within the organic ligand, such as 3D tetrahedral network, we can obtain:

$$\frac{\delta}{D} = \sqrt[3]{\sqrt{2}\,\Omega_T \left[\left(\frac{m_{glycerin}}{m_{NP}}\right)\left(\frac{\rho_{NP}}{\rho_{glycerin}}\right) + 1\right]} - 1, \quad (6)$$

where $\Omega_T \approx 0.55$ is the solid angle subtended by a regular tetrahedron at any of its vertices. Since δ/D depends only on the ratios of the mass and density of the glycerin and the hematite NPs, δ/D is expected to remain constant. To corroborate it, in this work, we used the ratios $m_{glycerin}/m_{NP} = 1$ and $\rho_{NP}/\rho_{glycerin} \approx 4.2$ [37, 38], therefore, $\delta/D \approx 0.59$. From here, we can say that the parameter δ is roughly proportional to the particle size. The values of δ obtained for the studied samples are listed in table 2 (fifth column).

Since S_r is exponentially dependent on $\Delta E_A = E_A^{(a)} - E_A^{(v)}$, knowing the values of the activation energies for each sensor and for each working atmosphere will allow a better understanding of the sensor's operating mechanism. Using the particle size D and δ values, the activation energy,
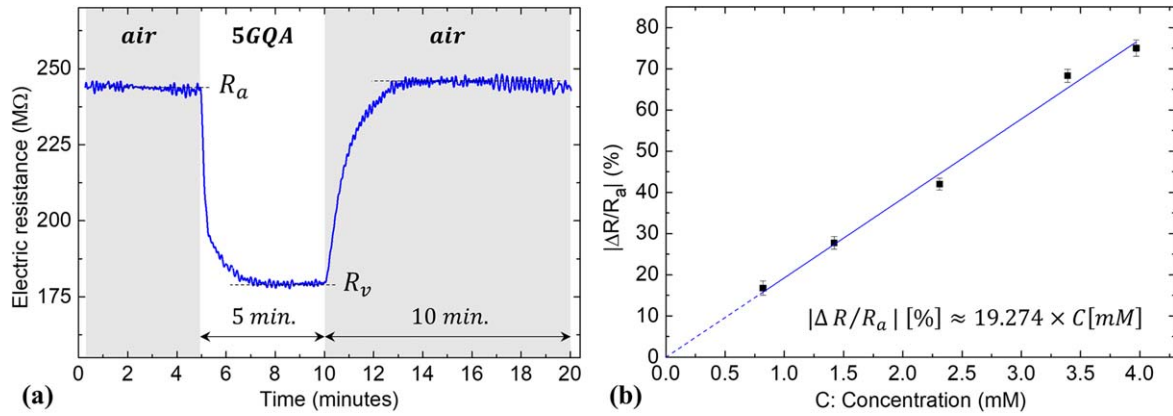
Figure 8. (a) Room-temperature time-dependence of the electrical resistance of the sensor based on S-800 sample. The gray region (white region) corresponds to air atmosphere (5GQA atmosphere). (b) 5GQA concentration-dependence of $|\Delta R/R_{\mathrm{a}}|$ in the range from 0.8 to 4.0 mM obtained for sample S-800.
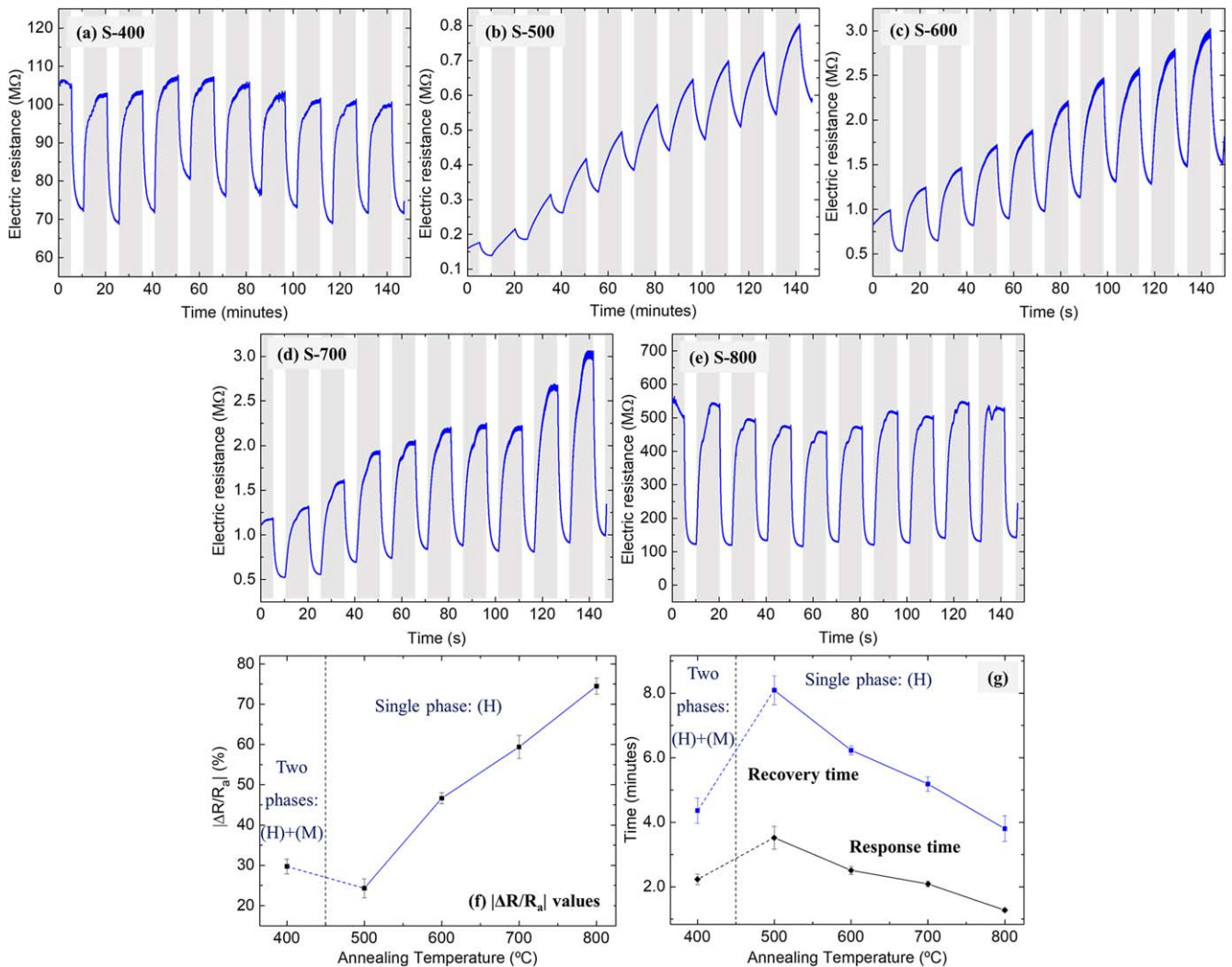
Figure 9. (a)–(d) Room-temperature time-dependence of the electrical resistance of the sensor during the cyclically changed atmosphere: from air atmosphere (gray region) to 5GQA atmosphere (white region). (e) $|\Delta R/R_{\mathrm{a}}|$ sensitivity values of the samples annealed at different temperatures (5GQA concentration of $C \approx 4$ mM). (f) Response and recovery times determined from the electrical resistance changes of the samples annealed at different temperatures.
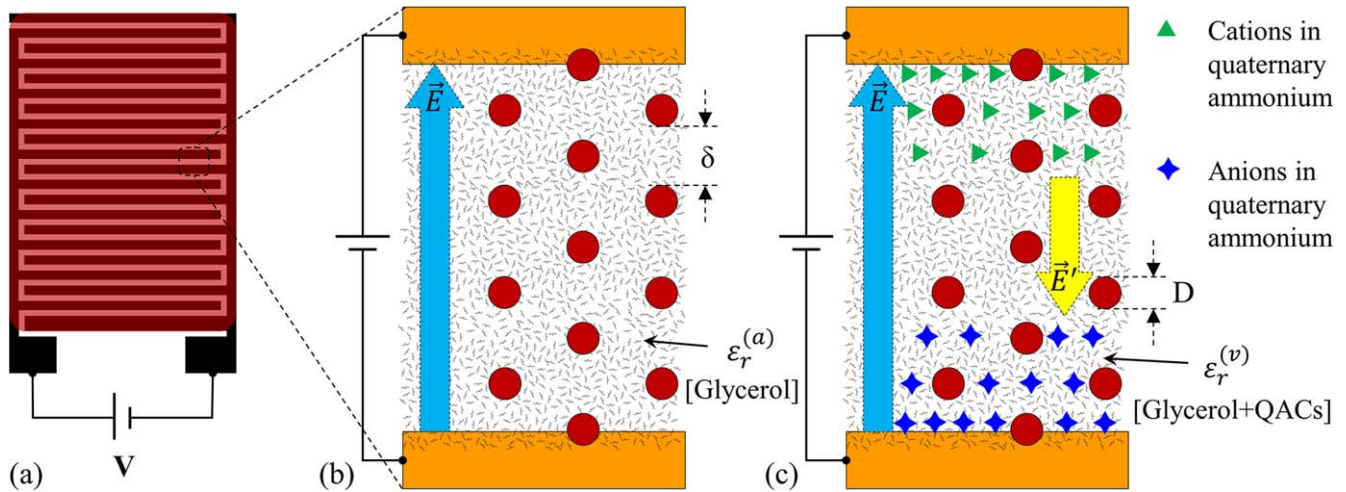
Figure 10. (a) Schematic representation of the sensor connected to a power source. A small portion of the sensor (not to scale) in (b) air atmosphere and (c) in a 5GQA vapor are represented schematically to exemplify the operating mechanism.

Table 2. Summary of the estimated parameters involved in the proposed sensor operating mechanism. Only the single-phase NPs are considered (S-500 to S-800). The meaning of each parameter is described throughout the text.

Sample	S_r	ΔE_A (kJ mol^{-1})	D_{XRD}(nm)	δ (nm)	$E_A^{(a)}$ (kJ mol^{-1})	$E_A^{(v)}$ (kJ mol^{-1})	S_{proj}/V (μm^{-1})	$t_{response}$ (min.)	$t_{recovery}$ (min.)
S-500	1.32	0.68	23.5	13.9	1.73	1.06	63.8	3.52	8.09
S-600	1.88	1.54	25.2	14.9	1.62	0.08	59.6	2.51	6.23
S-700	2.47	2.20	41.4	24.5	0.98	−1.22	36.2	2.09	5.19
S-800	3.94	3.34	66.9	39.6	0.61	−2.73	22.4	1.28	3.80

$E_A^{(a)}$ can be estimated using equation (5). Because the dielectric constant of the organic ligand in air remains constant ($\varepsilon_r^{(a)} \approx 47$ [39]), the activation energy is expected to depend only on the diameter of the NPs, thus, the increase in D contributes to reducing the parameter $E_A^{(a)}$, as shown in the sixth column of table 2.

The scenario is modified when the material sensor is exposed to the presence of 5GQA-vapor. To evidence this, the values for $E_A^{(v)}$ are estimated by substituting the values of ΔE_A and $E_A^{(a)}$ in equation (4), and the obtained values are listed in the seventh column of table 2. As expected, positive values of $E_A^{(v)}$ are obtained for the sensors based on S-500 and S-600 samples. However, negative $E_A^{(v)}$ values are found for the sensors based on S-700 and S-800 samples. In order to find a plausible explanation for that striking result, we proposed the following:

(i) Sensors based on S-500 and S-600 samples: for those sensors, it is observed that the $E_A^{(v)}$ values are lower for sensors based on larger diameter NPs, as expected from the expression equation (5). Also, it is also observed that the activation energy in the presence of 5GQA-vapor is lower than the corresponding value in the presence of air ($E_A^{(v)} < E_A^{(a)}$). As the geometrical parameters remain the same in each sensor, from equation (5), it follows that the lower activation energy of the sensors under the influence of 5GQA-vapor is due to the increase in the dielectric constant of the

organic ligand due to the incorporation of ions from the 5GQA-vapor in the organic matrix. Furthermore, according to the operating scheme proposed in figures 10(a)–(c), the ions coming from the 5GQA will have a greater effect on the sensor that allows them easier migration, that is, the sensor that contains larger NPs, due to the degree of opposition to the ions migration is inversely related to the NPs size (as will be discussed later quantitatively). Thus, the effect of the size of NPs added to the effect of the 5GQA-vapor in the dielectric constant value of the organic ligand, generates a change in the activation energy such that, $\Delta E_{A(S-500)} < \Delta E_{A(S-600)}$, thus leading to the sensitivity improvement of the sensor based on S-600 sample with respect to sensor based on S-500 sample.

(ii) Sensors based on S-700 and S-800 samples: Sensors based on hematite NPs with a size larger than $D \sim 26$ nm drive to negative activation energy when the sensors are exposed to 5GQA-vapor, that is, $E_A^{(a)} > 0$ and $E_A^{(v)} < 0$, which is intriguing. According to the model proposed by Neugebauer and Webb (equation (2)), the electrical resistance of the sensor decreases by increasing the operating temperature, which corresponds to a material showing a semiconductor-like behavior. It seems to be the case when the sensor is exposed to air atmosphere. The negative value of the activation energy when the sensors in exposed to 5GQA-vapor, suggest that equation (2) is not more applicable. It means that sensors composed of

hematite NPs with a mean size larger than $D \sim 26$ nm no longer follow the semiconductor-type conduction mechanism, but they likely behave as metallic-like. Although that 'pseudo' semiconductor-to-metal transition seems to be triggered by the increase of the hematite NPs size, additional studies are needed to determine the exact role of the particle size on the operation mechanism of this type of sensor, since it directly affects the sensing response to 5GQA-vapors.

Regarding the response time and recovery time, these parameters mainly depend on the facility that the long chains of the QACs (cationic chains) can migrate within the organic ligand by the action of the electric field, which can be hampered by the presence of the hematite NPs. We considered that the parameter which quantifies the degree of obstruction is only geometrical, and it is related to the projected area of the NPs (S_{proj}) perpendicular to the migration path of QACs molecules, and to the volume of NPs (V) according to: $S_{proj}/V = \left(\frac{\pi}{4}D^2\right)/\left(\frac{\pi}{6}D^3\right) = \frac{2}{3D}$. The estimated S_{proj}/V, t_{response} and t_{recovery} values are listed in table 2. As observed, a direct relationship of both t_{response} and t_{recovery} with the S_{proj}/V parameter is evidenced, thus reinforcing the validity of the proposed approach about of degree of obstruction provoked by the NPs.

4. Conclusions

We have successfully designed and prototyped a novel resistive gas sensor composed of monophasic hematite NPs. A proof of concept using quaternary ammonium compounds vapors as testing gas provided encouraging results, with a lower concentration threshold of ≈ 1 mM. By using NPs of different sizes, degree of crystallinity, and surface defects we have established that the sensor sensitivity depends on the polar (dielectric) properties of the organic ligand, more than the electrical properties of the hematite NPs. Although the detection limits of ≈ 1 mM can be considered competitive, our results suggest that the sensitivity can be improved: (i) by a better control of the particle size polydispersity and a better tuning of the dielectric properties of the organic ligand. (ii) By promoting changes in electrical conduction mechanism, as in sensors based on samples S-700 and S-800. In the latter case, the microstructural parameters seem to meet a certain condition that enables a semiconductor-to-metal like transition provoked by the change of atmosphere from air to QACs vapor. This latter aspect merits deeper studies to unambiguously establish the role of both intrinsic and topological factors in the final sensor performance.

Acknowledgments

Data availability statement

All data that support the findings of this study are included within the article (and any supplementary files).

Conflict of interest

The authors declare no conflict of interest.

ORCID iDs

Luis T Quispe ⬤ https://orcid.org/0000-0003-0824-4184
A A Baldárrago-Alcántara ⬤ https://orcid.org/0000-0003-4946-2962
L León Félix ⬤ https://orcid.org/0000-0001-9392-4592
J A Fuentes-García ⬤ https://orcid.org/0000-0003-4952-3702
D G Pacheco-Salazar ⬤ https://orcid.org/0000-0003-4685-2244

References

[1] EPA 2018 Product performance test guidelines: disinfectants for use on environmental surfaces, guidance for efficacy testing, Ocspp 810.2200, no. February, pp 1–19(https://www.epa.gov/test-guidelines-pesticides-and-toxic-substances)

[2] Rutala W A, White M S, Gergen M F and Weber D J 2006 Bacterial contamination of keyboards: efficacy and functional impact of disinfectants *Infect. Control Hosp. Epidemiol.* **27** 372–7

[3] Luz A, DeLeo P, Pechacek N and Freemantle M 2020 Human health hazard assessment of quaternary ammonium compounds: didecyl dimethyl ammonium chloride and alkyl (C12–C16) dimethyl benzyl ammonium chloride *Regul. Toxicol. Pharmacol.* **116** 104717

[4] DeLeo P C, Huynh C, Pattanayek M, Schmid K C and Pechacek N 2020 Assessment of ecological hazards and environmental fate of disinfectant quaternary ammonium compounds *Ecotoxicol. Environ. Saf.* **206** 111116

[5] Lim X Z 2020 Special to C&EN, 'Questioning quats' safety *C&EN Glob. Enterp.* **98** 28–33

[6] Osimitz T G and Droege W 2021 Quaternary ammonium compounds: perspectives on benefits, hazards, and risk *Toxicol. Res. Appl.* **5** 239784732110490

[7] Maher B 2008 Lab disinfectant harms mouse fertility *Nature* **453** 964

[8] Cayo-Rojas C and Medrano-Colmenares S 2021 Fifth generation quaternary ammonium in dentistry: effective against sars-cov-2? *J. Oral Res.* **10** 1–4

[9] Baumes L A, Sogo M B, Montes-Navajas P, Corma A and Garcia H 2009 First colorimetric sensor array for the identification of quaternary ammonium salts *Tetrahedron Lett.* **50** 7001–4

[10] Kurrey R, Deb M K and Shrivas K 2019 Surface enhanced infra-red spectroscopy with modified silver nanoparticles (AgNPs) for detection of quaternary ammonium cationic surfactants *New J. Chem.* **43** 8109–21

[11] Al-Hashem M, Akbar S and Morris P 2019 Role of oxygen vacancies in nanostructured metal-oxide gas sensors: a review *Sensors Actuators B* **301** 126845

[12] Zhang S *et al* 2019 Highly-sensitivity acetone sensors based on spinel-type oxide (NiFe$_2$O$_4$) through optimization of porous structure *Sensors Actuators B* **291** 266–74

[13] Xiong Y, Zhu Z, Ding D, Lu W and Xue Q 2018 Multi-shelled ZnCo$_2$O$_4$ yolk-shell spheres for high-performance acetone gas sensor *Appl. Surf. Sci.* **443** 114–21

[14] Chen J, Xu L, Li W and Gou X 2005 α-Fe$_2$O$_3$ Nanotubes in gas sensor and lithium-ion Battery applications *Adv. Mater.* **17** 582–6

[15] Zhang F *et al* 2009 Controlled synthesis and gas-sensing properties of hollow sea urchin-like α-Fe$_2$O$_3$ nanostructures and α-Fe$_2$O$_3$ nanocubes *Sensors Actuators B* **141** 381–9

[16] Tan J, Chen J, Liu K and Huang X 2016 Synthesis of porous α-Fe$_2$O$_3$ microrods via *in situ* decomposition of FeC$_2$O$_4$ precursor for ultra-fast responding and recovering ethanol gas sensor *Sensors Actuators B* **230** 46–53

[17] Qiang Z *et al* 2016 Solvothermal synthesis of 3D leaf-like α-Fe$_2$O$_3$ and its gas-sensing properties research *Mater. Lett.* **181** 29–33

[18] Garcia D, Picasso G, Hidalgo P, Peres H E M, Sun Kou R and Gonçalves J M 2017 Sensors based on Ag-loaded hematite (α-Fe$_2$O$_3$) nanoparticles for methyl mercaptan detection at room temperature *Anal. Chem. Res.* **12** 74–81

[19] Ghutepatil P R and Pawar S H 2020 Structural, morphological, magnetic and self-heating studies of one-step polyol synthesized manganese ferrite (MnFe$_2$O$_4$) nanoparticles *Int. J. Nanosci.* **19** 1950003

[20] Mohammadi A and Barikani M 2014 Synthesis and characterization of superparamagnetic Fe$_3$O$_4$ nanoparticles coated with thiodiglycol *Mater. Charact.* **90** 88–93

[21] Sivakumar P, Ramesh R, Ramanand A, Ponnusamy S and Muthamizhchelvan C 2011 Synthesis and characterization of nickel ferrite magnetic nanoparticles *Mater. Res. Bull.* **46** 2208–11

[22] Mendoza Santa Cruz G 2021 Degradación de tintas tóxicas a partir de nanocompósitos fotocatalíticos basados en ferritas magnéticamente separables, Universidad de Chile, Santiago de Chile (http://repositorio.uchile.cl/handle/2250/180184) (Accessed: 13 September, 2021)

[23] Dar M I and Shivashankar S A 2014 Single crystalline magnetite, maghemite, and hematite nanoparticles with rich coercivity *RSC Adv.* **4** 4105–13

[24] Wu W, Jiang C Z and Roy V A L 2016 Designed synthesis and surface engineering strategies of magnetic iron oxide nanoparticles for biomedical applications *Nanoscale* **8** 19421–74

[25] Sanders J P and Gallagher P K 2003 Thermomagnetometric evidence of γ-Fe$_2$O$_3$ as an intermediate in the oxidation of magnetite *Thermochim. Acta* **406** 241–3

[26] Scott D W 2009 Sturges' rule *WIREs Comput. Stat.* **1** 303–6

[27] Jain S, Shah J, Negi N S, Sharma C and Kotnala R K 2019 Significance of interface barrier at electrode of hematite hydroelectric cell for generating ecopower by water splitting *Int. J. Energy Res.* **43** 4743–55

[28] Farhanian D, De Crescenzo G and Tavares J R 2018 Large-scale encapsulation of magnetic iron oxide nanoparticles via syngas photo-initiated chemical vapor deposition *Sci Rep.* **8** 12223

[29] Iacovita C *et al* 2015 Polyethylene Glycol-mediated synthesis of cubic iron oxide nanoparticles with high heating power *Nanoscale Res. Lett.* **10** 391

[30] Bora D K, Braun A, Erat S, Safonova O, Graule T and Constable E C 2012 Evolution of structural properties of iron oxide nano particles during temperature treatment from 250 °C–900 °C: x-ray diffraction and Fe K-shell pre-edge x-ray absorption study *Curr. Appl. Phys.* **12** 817–25

[31] Zhang C *et al* 2015 Quaternary ammonium compounds (QACs): a review on occurrence, fate and toxicity in the environment *Sci. Total Environ.* **518–519** 352–62

[32] Wade A and Weller P J 1994 *Handbook of Pharmaceutical Excipients* 2nd edn (London: American Pharmacists Association)

[33] Matthew J W, Ellenhorn J, Schonwald S and Ordog G 1997 *Ellenhorn's Medical Toxicology* 2nd edn (Maryland, USA: Diagnosis and Treatment of Human Poisoning)

[34] Evans S D, Johnson S R, Cheng Y L and Shen T 2000 Vapour sensing using hybrid organic-inorganic nanostructured materials *J. Mater. Chem.* **10** 183–8

[35] Ibañez F J and Zamborini F P 2012 Chemiresistive sensing with chemically modified metal and alloy nanoparticles *Small* **8** 174–202

[36] Franke M E, Koplin T J and Simon U 2006 Metal and metal oxide nanoparticles in chemiresistors: does the nanoscale matter? *Small* **2** 36–50

[37] Volk A and Kähler C J 2018 Density model for aqueous glycerol solutions *Exp. Fluids* **59** 75

[38] National Center for Biotechnology Information 2022 PubChem, Hazardous Substances Data Bank (HSDB): 2964 —PubChem (https://pubchem.ncbi.nlm.nih.gov/source/hsdb/2964)

[39] Mahmud S N S, Jusoh M A, Yeow Y K, Esa F and Sutjipto A G E 2017 complex permittivity determination of glycerol using graphical and numerical technique *Aust. J. Basic Appl. Sci.* **11** 172–9